Title

Evaluation of the BreastSimulator software platform for breast tomography

Permalink

https://escholarship.org/uc/item/5zc2v7ns

Journal

Physics in Medicine and Biology, 62(16)

ISSN

0031-9155

Authors

Mettivier, G
Bliznakova, K
Sechopoulos, I
et al.

Publication Date

2017-08-21

DOI

10.1088/1361-6560/aa6ca3

Copyright Information

Peer reviewed

Evaluation of the *BreastSimulator* software platform for breast tomography

G. Mettivier[1], **K. Bliznakova**[2], **I. Sechopoulos**[3,4], **J. M. Boone**[5], **F. Di Lillo**[1], **A. Sarno**[1], **R. Castriconi**[1], and **P. Russo**[1]

[1]Università di Napoli Federico II, Dipartimento di Fisica "Ettore Pancini", and INFN Sezione di Napoli, I-80126 Napoli, Italy [2]Department of Electronics, Technical University of Varna, Varna, Bulgaria [3]Dutch reference centre for screening (LRCB), PO Box 6873, 6503 GJ Nijmegen, The Netherlands [4]Department of Radiology and Nuclear Medicine, Radboud University Medical Centre, P.O. Box 9101, 6500 HB Nijmegen, The Netherlands [5]Department of Radiology, University of California, Davis, Medical Center, Sacramento, California, USA

Abstract

The aim of this work is the evaluation of the software *BreastSimulator*, a breast X-ray imaging simulation software as a tool for the creation of 3D uncompressed breast digital models and for the simulation and the optimization of computed tomographic (CT) scanners dedicated to the breast. Eight 3D digital breast phantoms were created with glandular fraction in the range 10% to 35%. The models are characterised by different sizes and modelled realistic anatomical features. X-ray CT projections were simulated for a dedicated cone-beam CT scanner and reconstructed with the FDK algorithm. X-ray projection images were simulated for 5 mono-energetic (27, 32, 35, 43 and 51 keV) and 3 poly-energetic X-ray spectra typically employed in current CT scanners dedicated to the breast (49, 60, or 80 kVp). Clinical BCT images acquired from two different clinical breast CT scanners were used for comparison purposes. The quantitative evaluation included calculation of the power-law exponent, β, from simulated and real breast tomograms, based on the Power Spectrum (NPS) fitted with a function $S(f) = \alpha/f^{\beta}$. The breast models were validated by comparison against clinical breast CT and published data. The calculated β coefficients are close to that of clinical CT data from a dedicated breast CT scanner and reported data in the literature. In this paper we evaluated the software package *BreastSimulator* to generate breast models suitable for use with breast CT imaging The breast phantoms produced with the software tool can reproduce the anatomical structure of real breasts, as evaluated by calculating the β exponent from the power spectral analysis of simulated images. As such, this research tool will contribute considerably to the further development, testing and optimisation of breast CT imaging technique.

Keywords

Breast CT; Simulation; Breast Model; Anatomical structure

Corresponding author: Giovanni Mettivier, PhD, Università di Napoli Federico II, Dipartimento di Fisica "Ettore Pancini", Compl. univ. Monte S. Angelo, Via Cintia, I-80126 Napoli, Italy, ph.: +39-081-676137, mettivier@na.infn.it.

1. Introduction

Mammography, and in particular digital mammography (DM), is a fundamental imaging technique in breast cancer screening and diagnosis. DM returns a two-dimensional (2D) digital representation of a compressed three-dimensional (3D) object. Therefore, tissues belonging to different planes are all projected on the same X-ray image plane, making it difficult to detect possible abnormalities. This condition may be even worse in dense breasts, characterized by a high fraction of glandular tissue. In recent years, digital breast tomosynthesis (DBT) has been introduced as a form of 3D imaging for screening and clinical diagnosis of the compressed breast in order to overcome this limitation (Sechopoulos 2013). On the other hand, cone-beam computed tomography (CT) scanners dedicated to the uncompressed breast (breast CT, BCT) are available either experimentally or commercially, characterized by the use of quasi-mono-energetic [McKinley *et al* 2005] or poly-energetic X-ray beams [Lindfords *et al* 2008; O'Connell *et al* 2010; Kalender *et al* 2012; Russo et al 2010; Mettivier *et al* 2011; Sarno *et al* 2015, 2016a]. Parallel-beam synchrotron radiation mono-energetic BCT is also under investigation [Longo *et al* 2016; Mettivier *et al* 2016; Sarno *et al* 2016b]. But before the BCT can become a clinical procedure a number of issues should be optimized, such as the source and the detector design [Kalender *et al* 2012], the acquisition strategy [Linfords *et al* 2008; McKinley *et al* 2012], the reconstruction methods. To perform such investigations, there is a strong need of large databases of clinical images. Alternatively, images may be simulated from computational 3D digital breast models. They can be classified as digital phantoms based on patient data or mathematical data. In BCT, simple mathematical breast phantoms, usually in the form of cylinder, half-ellipsoid or slabs of homogeneous material with a given glandular to adipose breast ratio, are widely used in simulations particularly for dosimetry and optimization of acquisition geometry [Boone *et al* 2004; Mettivier *et al* 2016; Lanconelli *et al* 2013]. However, when it is necessary to investigate parameters such as the detectability of lesions, the performance of image processing algorithms or the reconstruction algorithms, the use of a homogeneous background is a limitation, since the anatomical structure is not reproduced.

Mathematical breast phantoms for BCT may be produced also with the *BreastSimulator* software tool [Bliznakova *et al* 2003], which is a software application dedicated for research in X-ray breast imaging. This research tool allows to create realistic 3D uncompressed breast models. The simulation of the breast compression adopted during DM and DBT, is also included (Zyganitidis *et al.* 2007). With this software, it is possible to simulate mammographic, tomosynthesis and fully tomographic breast imaging geometries. The *BreastSimulator* tool was previously validated and evaluated as a reliable tool for the simulation of DM systems [Bliznakova *et al* 2010].

The purpose of this study was to validate this software tool as an appropriate X-ray simulator for dedicated BCT imaging. This investigation is based on the quantification of the anatomical noise, evaluated by calculating the β exponent deduced from the power spectral analysis of the CT simulated images. The closeness of the power spectrum coefficient β (calculated from simulated CT images) to that calculated from clinical CT images of the

uncompressed breast, was the criterion for validating *BreastSimulator* for 3D breast imaging studies.

2. Materials and methods

2.1 BreastSimulator

The main components of the *BreastSimulator* [Bliznakova *et al* 2012] are the module for the creation of breast composition models and the module for the simulation of X-ray imaging.

2.1.1 Breast model generation module—This module was used to generate breast models of given size and composition. The simulated breast features include the breast shape, the duct system, the Cooper's ligaments, the pectoralis muscle, the 3D mammographic texture, the skin, the lymphatic and blood systems and breast abnormalities (masses and calcifications). Additionally, a 3D texture matrix was created to simulate breast structures not explicitly modelled, such as nerves and blood vessels, as well as to increase the realism of the simulated ligaments. The user can increase the complexity of the breast model by including any such features and by increasing their number (e.g. simulating a large number of Cooper's ligaments, or of lactiferous ducts) or size (e.g., by simulating short-sized or long-sized ducts). The aim was to simulate the complexity of the actual breast anatomies, as found for samples women with different glandular fraction, breast size and shape, and anatomical texture. An example of a simulated breast phantom with and without Cooper ligaments is shown in figure 1a,b, respectively.

The duct system is simulated as a network of cylinders (figure 1a), marked as a fibrous tissue and probabilistically arranged in the breast in a tree-like arrangement. The duct model includes the major ducts and the lactiferous ducts. Cooper ligaments are simulated as thin ellipsoidal shells, originating at randomly sampled positions in the breast model (figure 1b). Their linear attenuation coefficient (at the given X-ray photon energy) is equal to that of the ducts, while the compartments enclosed by them are assigned the attenuation coefficient of the breast adipose tissue. A mixture of adipose, fibrous and connective tissues as well as other non-glandular tissue types not explicitly modelled, simulate the mammographic texture. The algorithm for generating this texture is based on the use of random walk, following the concept of the "fractional Brownian motion model". The pectoralis muscle (figure 1a) is approximated as a cone-shaped object. Breast abnormalities are modelled with round, ovoid, elongated or irregular shapes.

2.1.2 X-ray imaging module—The X-ray imaging module contains information for the acquisition geometry and allows for setting acquisition parameters like source-to-detector (SDD) and source-to-isocenter (SID) distances, number of projection images, gantry angles, beam energy and detector type. X-ray projection images were obtained by simulating the transport of mono-energetic X-ray photons in the breast model. Image formation was based on the Lambert-Beer's law for X-ray attenuation. Figure 2 shows the BCT acquisition geometry used in the present simulation study. X-ray tracing was based on the Siddon's algorithm to calculate the exact radiological path through voxels. Poisson quantum noise was added to the noise-free projection images, using a Gaussian random number generator, with a variance equal to the number of photons incident on each detector pixel. For

simulating poly-energetic beams, the images obtained at each spectra energy were subjected to weighted sum based on the corresponding photon fluence of the X-ray spectrum adopted for the simulation.

2.2 Setup description

For the imaging setup, we simulated a cone-beam irradiation geometry, with SID and SDD set to 458 mm and 866 mm, respectively. The detector was modelled with a size of 700×700 pixels, while the pixel size was set to 0.333 mm, in the order of the effective pixel size adopted in projection images with clinical BCT scanners (Boone *et al* 2005). Photon scatter in the breast and detector response were not simulated. In particular, scatter in uncompressed breasts, though significant, introduces a low-frequency trend on the spatial variation of the background signal, at frequencies below the minimum spatial frequency (0.05 mm^{-1}) here considered in the analysis of the NPS for evaluation of the power-law exponent, β (Mettivier *et al* 2010).

We note that considering scatter-free views of the simulated breast may introduce a decrease of the noise power at low frequencies in CT slices, so producing a decrease of the power-law magnitude, α. However, for the purpose of this work, only the power-law exponent, β, will be analysed. On the other hand, both α and β will be considered as free parameters in the linear fit of the log(PS) curve $\log[S(f)] = (\log \alpha) - \beta \cdot f$ in the analysis of the radial PS from simulated or measured CT slices.

For each projection and photon energy, a number of 10^7 photon histories were run. Simulated images were generated for all incident mono-energetic beams with energy in the range 15–80 keV, with 1-keV increments. In the case of poly-energetic beams, for each energy we run a code to produce three projection images from the initial x-ray spectra and for each gantry angle. These three projection images have pixel values representing distances in mm ($d_{adipose}$, d_{gland}, d_{skin}) as the travelled distance of the x-ray through (a) the adipose tissue, (b) the gland tissue and (c) the skin, respectively. A total of 70200 projections were obtained for the 80-kVp poly-energetic spectrum, while for the 49-kVp and 60-kVp spectra this number was 36720 and 48600, respectively. Then, the corresponding image per gantry angle was obtained as follows:

$$polyimage = \sum_{E=0}^{E_{end},keV} w_E . E . exp\left(-\mu(E)_{adipose} . d_{adipose} - \mu(E)_{gland} . d_{gland} - \mu(E)_{skin} . d_{skin}\right)$$

where w_E, $\mu(E)_{adipose}$, $\mu(E)_{gland}$, and $\mu(E)_{skin}$ are the weighting coefficient calculated based on the incident x-ray spectra and the attenuation coefficient for the corresponding tissue and energy, respectively.

CT scans with 360 angular views were simulated, with mono-energetic (27, 32, 35, 43 and 51 keV) as well as poly-energetic X-ray spectra (49, 60, or 80 kVp). These spectra correspond to the spectra used for patient scans performed with the breast CT scanners at University of California Davis Medical Center (UCDMC) (Lindfors *et al* 2008; Gazy and Boone 2014), and the commercial scanner of Koning Ltd. (O'Connell *et al*) also used at

Radboud University Medical Center (RUMC). The spectra were calculated using the spectral model by Boone *et al* 1997. The beam qualities were: (49 kVp, 1.39 mm Al) (Sechopoulos *et al* 2010); (60 kVp, 4.26 mm Al) (80 kVp, 5.74 mm Al) (Boone *et al* 2005). CT scans for mono-energetic beams with photon energies of 32 keV, 43 keV and 51 keV were simulated, since these energies correspond to the mean energy of the poly-energetic spectra at 49, 60 and 80 kVp, respectively. On the other hand, mono-energetic beams at 27 keV and 35 keV have a photon energy close to those used in the experimental studies ongoing at the Elettra synchrotron radiation facility on phase-contrast BCT [Longo *et al* 2016].

Image pixel dimensions were 0.333 mm × 0.333 mm. The simulation of 360 X-ray projections took 24h for the mono-energetic beams on a dedicated personal computer (see below).

2.3 Breast phantoms

For the purpose of this work, we use *BreastSimulator* to create eight different 3D digital breast phantoms with realistic anatomical features (Breast models from #1 to #8, with different sizes and compositions). The research tool runs on an Intel Core 2 Quad Processor Q8200 2.33 GHz, with 8 GB RAM and 64 bit Linux operating system. The attenuation coefficients of the different breast components were derived from the XCOM Program (NIST Database). Table I shows the characteristics of each breast phantom (background matrix size, voxel dimensions, glandular fraction and breast size) and the corresponding simulated tissue features. The size (in pixels) of the 3D breast matrix ranges from $(560)^3$ for the Breast #2, to $(1000)^3$ for the breast models #4–#7. The voxel size of these matrices ranges from 0.1 mm to 0.25 mm (in each dimension) and the volume from 100 mm^3 (#4, #5 and #6) to 469 mm^3 (#1 and #8). As a result of simulating a certain breast anatomy, each breast model turns out to have a different glandular fraction by volume which varies from 10% to 35% (i.e., the glandular fraction is an output datum of the software). The breast models were generated free of lesions in order to avoid any bias in the results. Based on the breast model complexity, the CPU time for the realization of a digital breast model ranged from 15 to 30 min.

2.4 Clinical Data

In order to make a comparison with measured clinical data, the same procedure for the evaluation of β was applied on clinical BCT images acquired by the team at UCDMC and at RUMC. The data acquired with the UCDMC scanner are relative to a 180 breasts. The reconstructed slices have different dimensions with a voxel size of $0.20 \times 0.20 \times 0.35$ mm^2. Fig. 3 shows clinical CT views and 3D renderings of one of this sample acquired with the UCDMC scanner. For comparison, in figure 3 is shown a simulated breast model (#5) with the same glandular fraction.

The data acquired with the RUMC scanner include CT scans of eight different real breasts. The number of projections is 300 over 360 deg and the tube voltage was 49 kVp. The reconstructed slices have different dimensions with a voxel size of $0.27 \times 0.27 \times 0.27$ mm^3.

2.5 Assessment of the β parameter

It has been previously reported [Burgess *et al* 2001] that the anatomical structure in mammograms may represent a major impediment to lesion detectability and that it shows an isotropic power law spectrum of the form $S(f) = \alpha/(f^\beta)$. Here, α describes the magnitude of fluctuation in the signal power, f represents the radial frequency and β (the log spectrum slope) has a critical role in determining the size at which a lesion reaches the threshold for detection [Chen *et al* 2012]. Its value (for natural scenes and for mammography) ranges between 1.5 and 3.5 [Burgess and Judy 2007] and its mean value has been reported to be approximately 3 for DM [Burgess *et al* 2001; Heine *et al* 1999] and approximately 2 for BCT [Metheany *et al* 2008; Chen *et al* 2012].

For the analysis of the β parameter, the projections of the simulated uncompressed breast were reconstructed with a commercial software (COBRA, Exxim Computing Corporation, Pleasanton, CA, USA) implementing the Feldkamp-Davis-Kress algorithm, providing axial, coronal and sagittal views. In order to evaluate the impact of slice thickness, the dimension of the reconstructed voxel was varied from $0.250 \times 0.250 \times 0.250$ mm^3 ($512 \times 512 \times 512$ voxels) to $0.250 \times 0.250 \times 2.00$ mm^3 ($512 \times 512 \times 64$ voxels). The power-law exponent β was derived from fitting the NPS functional form $S(f) = \alpha/(f^\beta)$ evaluated on ROIs selected randomly in reconstructed slices [Chen *et al* 2013]. A liner fit was applied to the radial log PS. Assuming uniform tissue characteristics in the various regions of the breast volume, one thousand ROIs have been selected randomly inside a single coronal slice or in the whole breast. A rejection method was used to insure that all ROIs were located within the breast anatomy on the image. Following the method of Metheany *et al* (2008), for each ROI, the mean pixel value was subtracted and then a Hanning window was applied. The ROI was chosen empirically while ensuring that it was large enough to allow for an accurate estimate of β but not too large so as to emphasize non-uniformities in the image. Then, the 2D NPS was computed by means of the Fast Fourier Transform for each ROI and the mean 2D PS was determined by averaging the PS from the 1000 ROIs. In order to obtain a 1D PS, a radial profile was evaluated. Finally, the β coefficient was calculated as the negative slope of the fitting line returned by computing a linear fit of log(1D PS) vs. log(f). The optimal frequency window (from f_1 to f_2) was selected for each PS(f), as the one which maximized the R^2 fit statistic, and the values of α and β were then recorded for each breast data set. We tested this method by evaluating the β coefficient of the 180 breast scans provided by UCDMC: figure 4a and 4b show the data obtained in this test. Specifically, fig. 4a shows the β values for all breasts, with the dashed line and the light grey shaded area showing the corresponding mean value ($\beta = 2.11$) and the range of data within $\pm$ 1 std. dev. (= 0.55), respectively. These values are also reported in the Tab. II. Fig. 4b shows the frequency distribution of the β values obtained for the UCDMC dataset.

3. Results

3.1 Breast Models

Figure 5 shows sample CT slices and the corresponding 3D renderings of all eight breast models created with *BreastSimulator* for this work, in the case of a simulated 80 kVp spectrum. In this figure, the different anatomical complexity explained in the various models

reflects into a different appearance of the simulated CT slices. In particular, the inclusions in model breasts of the Cooper's ligaments and of the varying-size duct system are clearly distinguishable features of the various breasts. The glandular tissue is well distinguished from the flat tissue as well as the skin tissue (when present).

3.2 Analysis of the power spectrum

After CT reconstruction of breast projections created with *BreastSimulator*, we evaluated the β coefficient from the resulting CT coronal slices (figure 6a,b); an example of PS plots and corresponding power-law fits is shown in figure 6c, together with PS data evaluated from clinical BCT scans at RUMC and UCDMC. The three illustrative cases shown in fig. 6c were randomly selected between the simulated phantoms; in the case of real breast from the UCDMC set we selected a case with a β parameter equal to the measured mean value. We observe that the *BreastSimulator* data show a different intercept, $\log(\alpha)$: indeed, the simulated data show a lower power, at all frequencies, than patient data. Measured β values for all the simulated and real breasts are reported in table II.

Tab. II reports the β coefficients calculated in the central coronal slice of each breast model described in table I, reconstructed with four thicknesses of the tomographic slice and for the different beam qualities. For instance, the results for a slice thickness of 0.250 mm and 0.500 mm are shown in fig. 7, for both mono-energetic (27, 32, 35, 43 and 51 keV) (fig. 7a,b) and poly-energetic (49, 50 and 80 kVp) spectra (fig. 7c,d).

We observe that the simulated projection images from computer breast models show a different value of the β coefficient, but for a given breast model, there is limited variation in the β values for varying energy of the X-ray beam. When considering the range of values found in UCDMC ($\beta = 2.11 \pm 0.55$), the data provided by *BreastSimulator* partially overlap this range, with breast models from #2 to #6 falling inside this range. As regards the change in β deriving from a different choice of the slice thickness in the CT reconstruction, the comparison of figs. 7a,b and 7c,d illustrates that there is a slight increase in β with the slice thickness increases. These considerations are confirmed also by the data in fig. 8 where the β coefficients are reported for all digital phantoms as a function of the beam energy for mono-energetic (fig. 8a) and poly-energetic (fig. 8b) spectra.

Figures 9a,bc,d show the β coefficients for each phantom for the 80 kVp poly-energetic spectrum as a function of the phantom glandularity. The continuous and dashed lines in the figure show the fitted value and range of ± 1 std. dev. reported in Chen *et al.* 2013, respectively.

Figure 10 shows the β coefficients as a function of slice thickness, calculated in the central coronal slice for breast models #1 to #8 for the 80 kVp poly-energetic setup. The area shaded in light gray represents the average value (dashed red line, $\beta = 1.86$) ± 1 std. dev. of the parameter β measured on clinical CT data reported by UCDMC on 44 breast images [Chen *et al* 2012]. It is observed that breast models #1 to #4 are totally outside this area and that models #5 to #8 are totally or in part within it. We also note that Chen *et al* 2013 at UCDMC evaluated the β coefficients from coronal CT slices on a cohort of 185 patients and they found a mean value $\beta = 1.96 \pm 0.46$.

Figure 11a shows the values of β computed in each reconstructed coronal slice from the chest-wall to the nipple (for a slice thickness of 0.250 mm), for phantom #5, for all mono-energetic as well as poly-energetic beams. The case of breast #5 was considered, since it shows the values of β (fig. 11) closest to the average value (1.96 ± 0.46) as reported by the UCDMC group [Chen *et al* 2013] and the our calculated mean value (2.11 ± 0.55). In fig. 11a, the values of β show some fluctuation with the slice position from chest wall to the nipple, however, independent parabolic fits to the data point relative to the six different beam qualities reveal a common trend, with β decreasing markedly toward the nipple and slightly decreasing also toward the chest wall. The simulated data for 80 kVp and for the corresponding 51 keV mono-energetic spectrum are replotted in fig. 11b, where it is seen that the two datasets of β values share the same mean value and standard deviation, for the slices along the longitudinal position from the chest wall to the nipple. A direct comparison between the β values within the simulated breast model #5 and a real patient scan (randomly selected), acquired with the RUMC scanner is shown in fig. 12. The X-ray spectra utilized for the simulation is the same used in the commercial scanner. A good agreement within the experimental uncertainty is obtained.

4. Discussion

The power spectrum analysis of simulated and clinical images suggests that the *BreastSimulator* generates breast models with a tomographic characteristic close to the real breast tomograms. Eight 3D uncompressed breast models characterized with different content, size and voxel resolution were created with the BreastSimulator software package. While the agreement between real and simulated β distributions is not to be taken as a paradigm for "correctness" of the anatomical structure of the 3D digital breast models, it is anyway a positive aspect of *BreastSimulator* that it is capable of reproducing the range of variability of this parameter found in patients' BCT scans. In this respect, we point out that the detailed distribution of the glandular tissue in the breast volume has no influence on the evaluation of the β parameter, since in the evaluation procedure (as reported in par. 2.5 and shown in fig. 6a,b) a large number of ROIs were selected randomly in the slice for computation of the average pixel value. Just for sake of example, the average β value plays the same role as the average glandular dose in breast dosimetry, where two different 3D distributions of the glandular dose might share the same MGD. It is the fraction of the glandular tissue that has an influence on the β value as reported in the literature (e.g. Chen *et al* 2013, Metheani *et al* 2008) and shown in fig. 9. This is reflected in fig. 3 where the spatial distributions of the glandular tissue in real and simulated breasts looks quite different, though the average β are comparable.

The creation of fatty, glandular and dense breast models is influenced by the simulated breast features: ducts, Cooper ligaments, adipose, fibrous and other connective tissues. For each phantom, we have simulated the tomographic acquisition with eight different setups (5 mono-energetic and 3 poly-energetic setups) and have obtained 64 CT reconstructions (fig. 5) with four slice thicknesses (0.250, 0.500, 1.000 and 2.000 mm) for a total of 256 CT reconstructions. The β coefficient for the slices in each reconstruction was calculated and reported in table II. The mean value and the standard deviation of calculated β values of simulated images (β ~2 for this 3D imaging modality) are in general in the range of the

calculated β values obtained for the clinical CT images from dedicated breast CT scanners. Published BCT data from a relatively large cohort of patients indicate an average β exponent between 1.86±0.38 and 1.96±0.46 [Metheani *et al* 2008; Chen *et al* 2013].

The increase of the thickness of the reconstructed slice results in an increase of the β values for each breast model and setup (table II and fig. 8) as expected due to the increase of the anatomical structure related to the higher thickness. This results are in agree with the data reported in Chen *et al* 2013 where an increase of the β value from 1.96 to 3.15 was due to the increase of the slice thickness (from 0.23 mm to 44 mm) and in Chen *et al* 2012.

The detailed comparison of β values calculated from simulated and real images (in fig. 7) shows that except breast models 1, 7 and 8 all other created breast phantoms have β values close to the β value calculated on the real images used in this study and are in the range of the β values reported in literature. In particular, we can note that the β value depends on the breast matrix size (from about 600^3 to 1000^3) and the voxel resolution (from 0.25 to 0.1 mm) as well as on the Cooper ligaments. Lower voxel resolution results in averaging of adipose and glandular tissues in one voxel. Lower voxel resolution combined with higher glandularity leads to slices with highly irregular structures which result in higher β values, as in the case of breast 1.

Increasing the voxel resolution has the opposite effect on β. If the parameters breast size and resolutions are well chosen and set, β values decrease with the decrease of the breast glandularity. These results are in agreement with the results reported also in Metheany *et al* 2008 and Chen *et al* 2013: in particular the data reported in fig. 8 and fig. 2 of these works, respectively. It was also observed that the β value depends on the number of simulated structures and anatomical details in the breast model. In particular, breast models #5 and #6 differ only in the number of the Cooper's ligaments and their initial radius. The increase of these ligaments leads to the increased β value. On the contrary, the β value is independent of the photon energy value (fig 10a) and tube kilovoltage (fig. 10b) in the mono-energetic and poly-energetic setup, respectively. This is expected, since the β value quantifies the anatomical structure in images.

Another aspect is highlighted by fig. 11. In the literature, there is no indication about the appropriate choice of the slice used for evaluation of the β parameter; in our study we assumed to use the central coronal slice, following Boone (Chen *et al* 2013). Results for β values calculated in all the slices are reported in fig 11. It can be observed the good agreement between these β values and those obtained for a real breast (fig. 12) as well as data reported by Engstrom *et al* 2009 in the case of tomosynthesis slices. The higher values of the β coefficients in the "central" slice in simulated data are due to the natural concentration of the glandular breast tissue around the nipple. This slice can be identified by a parabolic fit to the β values of each slice and considering the slice were the vertex of the parabola is found (see fig. 11a).

In this work, we used eight computer models of the breast with glandularity ranging between 10% and 35%. In the glandularity calculations, we included the skin. Four of the breasts had a glandular fraction of 10%, two had a glandular fraction of 24%, and two other breasts have

35% and 30% glandularity. The average glandularity was 23%, comparable to the value (19.3%) obtained by Yaffe et al. (2009) for the average glandularity obtained from 191 patient breast-CT images). Current efforts of our group are towards generating a very large number of computer models of the breast with different glandularity, sizes and dimensions, to be stored in a dedicated database and to be used for further research.

Regarding the computational time of about 24 hours, it includes a) generation of breast models, b) generation of 360 projection images and c) volume reconstruction. The most time-consuming part of the algorithm for generation of breast models is the part related to the generation of the Cooper ligaments. The locations of the Cooper ligaments are sampled randomly within the breast volume; then, a procedure verifies that the generated ligament does not have any intersection with other ligaments. At present, this process has not been optimised computationally, but we are working for reducing the time needed for their generation. Simulation for CT imaging was performed on two 6-core processor workstations, having 24-GB RAM. One projection image was simulated in about 4 minutes. Image formation simulation may be also optimised if cloud technology is used. On the other hand, the time for reconstructing tomograms was comparably negligible.

We are also working on the use of the *BreastSimulator* to simulate noise in projection images. Noise sources to be considered are the photon noise, the noise in the detector as well as the scattered X-rays. In these studies, a Monte Carlo code will be exploited to simulate X-ray interactions in the breast models and in the detectors. It is expected that simulated tomographic images with improved noise description will have characteristics closer to those from clinical scans. This future work will further establish the practical importance of *BreastSimulator* in carrying out feasibility studies in the field of breast X-ray imaging and in particular in advancing research and optimisation studies for breast CT.

5. Conclusions

This paper described the evaluation of a software package called *BreastSimulator* for research purposes in breast CT. Breast models of different size and content were simulated and the anatomical structure properties were evaluated by calculating the β exponent from the power spectral analysis of the simulated images. The good agreement between simulated and measured β in four clinical scans indicates the potential of *BreastSimulator* in devising digital phantom for describing the complex anatomy of the female breast. It is expected that the increase in the complexity of the present models (e.g., increase of the number of tissue structures) for breast CT with *BreastSimulator* will produce an even better description of the corresponding complexity of the anatomical structure of the breast; this depends also on the computing power available for simulation. This would be particularly important for the description of dense breasts.

Acknowledgments

and does not necessarily represent the official views of the National Cancer Institute or the National Institutes of Health.

References

Bliznakova K, et al. A three-dimensional breast software phantom for mammography simulation. Phys Med Biol. 2003; 48:3699–719. [PubMed: 14680268]

Bliznakova K, Suryanarayanan S, Karellas A, Pallikarakis N. Evaluation of an improved algorithm for producing realistic 3D breast software phamtoms: Application of mammography. Med Phys. 2010; 37:5604–17. [PubMed: 21158272]

Bliznakova K, Sechopulos I, Buliev I, Pallikarakis N. BreastSimulator: A software platform for breast x-ray imaging research. J Biomed Graph Comp. 2012; 2:1–14.

Boone JM, Fewell TR, Jennings RJ. Molybdenum, rhodium, and tungsten anode spectral models using interpolating polynomials with application to mammography. Med Phys. 1997; 24:1863–74. [PubMed: 9434969]

Boone JM, Shah N, Nelson TR. A comprehensive analysis of DgNCT coefficients for pendant-beometry cone-beam breast computed tomography. Med Phys. 2004; 31:226–235. [PubMed: 15000608]

Boone JM, Kwan ALC, Seibert JA, Nelson TR. Technique factors and their relationship to radiation dose in pendant geometry breast CT. Med Phys. 2005; 22:3767–3776.

Burgess AE, Jacobson FL, Judy PF. Human observer detection experiments with mammograms and power-law noise. Med Phys. 2001; 28:419–37. [PubMed: 11339738]

Burgess AE, Judy PF. Signal detection in power-law noise: Effect of spectrum exponents. J Opt Soc Am A. 2007; 24:B52–B60.

Chen L, Abbey CK, Nosratieh A, Lindfors KK, Boone JM. Anatomical complexity in breast parenchyma and its implications for optimal breast imaging strategies. Med Phys. 2012; 39:1435–41. [PubMed: 22380376]

Chen L, Abbey CK, Boone JM. Association between power law coefficients of the anatomical noise power spectrum and lesion detectability in breast imaging modalities. Phys Med Biol. 2013; 58:1663–81. [PubMed: 23422272]

Engstrom E, Reiser I, Nishikawa R. Comparison of power spectra for tomosynthesis projections and reconstructed images. Med Phys. 2009; 36:1753–1758. [PubMed: 19544793]

Heine JJ, Velthuizen. Spectral analysis of full field digital mammography data. Med Phys. 2002; 29:647–61. [PubMed: 12033559]

Kalender WA, Beister M, Boone JM, Kolditz D, Vollmar SV, Weigel MCC. High-resolution spiral CT of the breast at very low dose: Concept and feasibility considerations. Eur Radiol. 2012; 22:1–8. [PubMed: 21656331]

Lanconelli N, et al. Investigation of the dose distribution for a cone beam CT system dedicated to breast imaging. Phys Medica. 2013; 29:379–87.

Lindfors KK, Boone JM, Nelson TR, Yang K, Kwan ALC, Miller DF. Dedicated breast CT: Initial clinical experience. Radiology. 2008; 246:725–33. [PubMed: 18195383]

Longo R, Arfelli F, Bellazzini R, Bottigli U, Brez A, Brun F, et al. Towards breast tomography with synchrotron radiation at Elettra: first images. Phys Med Biol. 2016; 61:1634–49. [PubMed: 26836274]

McKinley RL, Tornai MP, Samei E, Bradshaw ML. Initial study of quasi-monochromatic X-ray beam performance for X-ray computed mammotomography. IEEE Trans Nucl Sci. 2005; 52:1243–50.

McKinley RL, Tornai MP, Tuttle LA, Steed D, Kuzmiak CM. Development and initial demonstration of a low-dose dedicated fully 3D breast CT system. Breast Imaging, Lecture Notes in Computer Science. 2012; 7361:424–33.

Metheany K, Abbey CK, Packard N, Boone JM. Characterizing anatomical variability in breast CT images. Med Phys. 2008; 35:4685–94. [PubMed: 18975714]

Mettivier G, Russo P, Lanconelli N, Lo Meo S. Evaluation of scattering in cone-beam breast computed tomography: A Monte Carlo and experimental phantom study. IEEE Trans Nucl Sci. 2010; 57:2510–17.

Mettivier G, Russo P, Cesarelli M, Ospizio R, Passeggio G, Roscilli L, Pontoriere G, Rocco R. Dedicated scanner for laboratory investigations on cone-beam CT/SPECT imaging of the breast. Nucl Instrum Meth A. 2011; 629:350–6.

Mettivier G, Fedon C, Di Lillo F, Longo R, Sarno A, Tromba G, Russo P. Glandular dose in breast computed tomography with synchrotron radiation. Phys Med Biol. 2016; 61:569–87. [PubMed: 26683710]

O'Connell A, Conover DL, Zhang Y, Seifert P, Logan-Young W, Lin CFL, Sahler L, Ning R. Cone-beam CT for breast imaging: Radiation dose, breast coverage, and image quality. Am J Roentgenol. 2010; 195:496–509. [PubMed: 20651210]

Russo P, Mettivier G, Lauria A, Montesi MC. X-ray cone-beam breast computed tomography: phantom studies. IEEE Trans Nucl Sci. 2010; 57:160–72.

Sarno A, Mettivier G, Russo P. Dedicated breast computed tomography: Basic aspects. Med Phys. 2015; 42:2786–804. [PubMed: 26127031]

Sarno A, Mettivier G, Di Lillo F, Cesarelli M, Bifulco P, Russo P. Cone-beam micro computed tomography dedicated to the breast. Med Eng Phys. 2016a; 38:1449–1457. [PubMed: 27727117]

Sarno A, Mettivier G, Golosio B, Oliva P, Spandre G, Di Lillo F, et al. Imaging performance of phase-contrast breast computed tomography with synchrotron radiation and a CdTe photon-counting detector. Phys Medica. 2016b; 32:681–690.

Sechopoulos I. A review of breast tomosynthesis. Part I. The image acquisition process. Med Phys. 2013; 40:014301. [PubMed: 23298126]

Sechopoulos I, Si Jia Feng S, D'Orsi CG. Dosimetric characterization of a dedicated breast computed tomography clinical prototype. Med Phys. 2010; 37:4110–20. [PubMed: 20879571]

Zyganitidis C, Bliznakova K, Pallokarakis N. A novel simulation algorithm for soft tissue compression. Med Bio Eng Comput. 2007; 45:661–669. [PubMed: 17551761]

Yaffe MJ, Boone JM, Packard N, Olonzo-Proulx O, Huang SY, Peressotti CL, Al Mayah A, Brock K. The myth of the 50-50 breast. Med Phys. 2009; 36:5437–5443. [PubMed: 20095256]
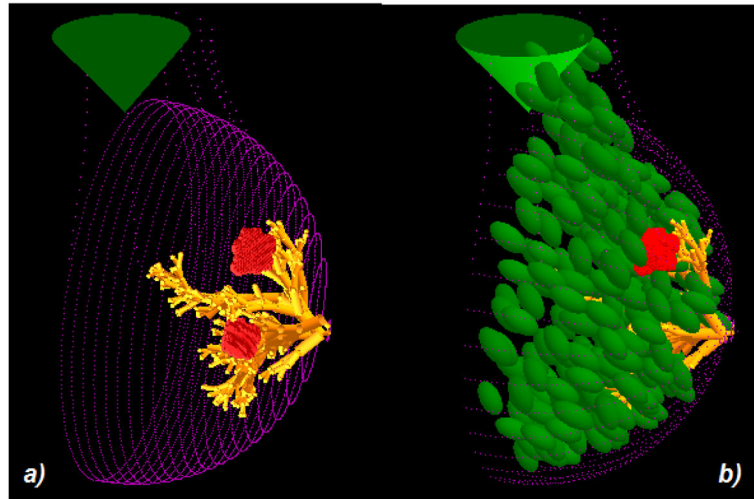
Figure 1.
Example of a simulated breast model containing two massive lesions (in red) and ductal system (in yellow), generated with the *BreastSimulator*: (a) model without and (b) with Cooper's ligaments (in green). The conical structure on the top of the breast simulates the pectoralis muscle.
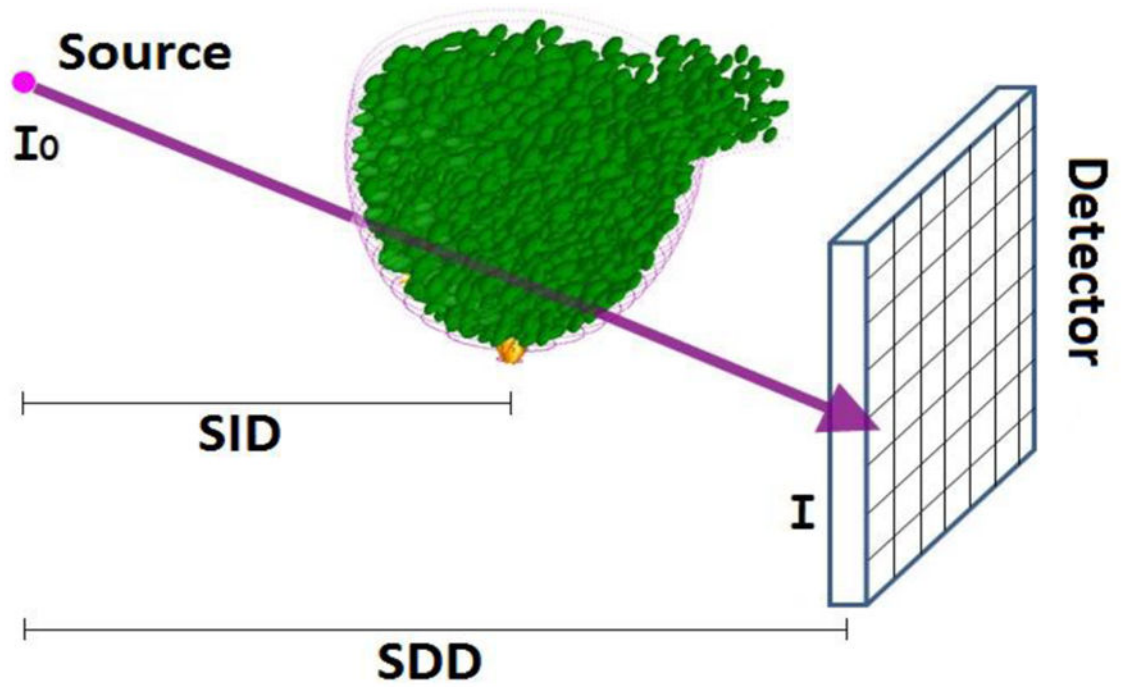
Figure 2.
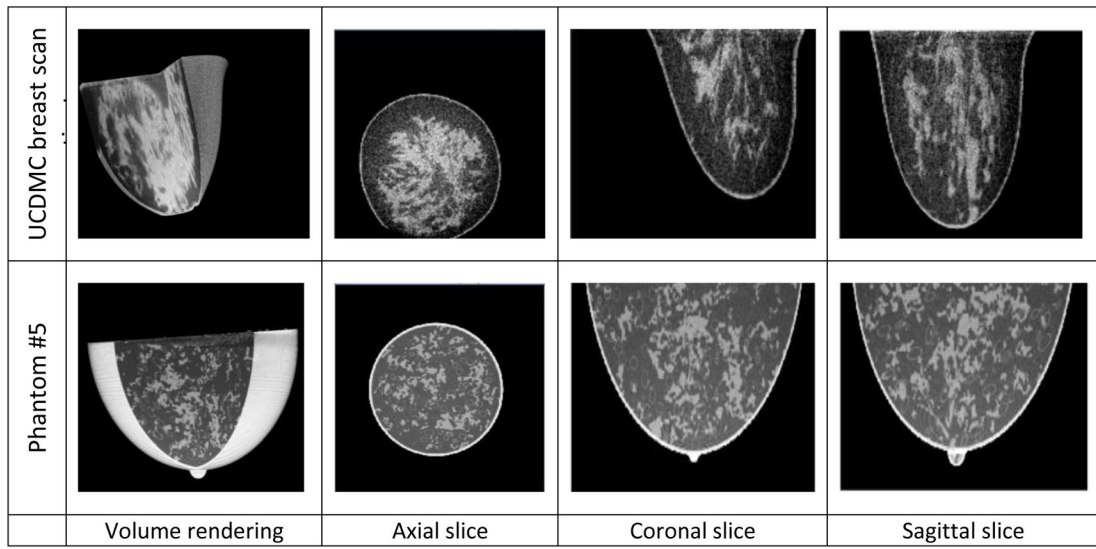Simulation of X-ray imaging with the X-ray imaging module.

Figure 3.
CT slices and corresponding 3D renderings of a real breast sample acquired with the UCDMC scanner (first raw) and a simulated breast phantom (model #5) (second raw).
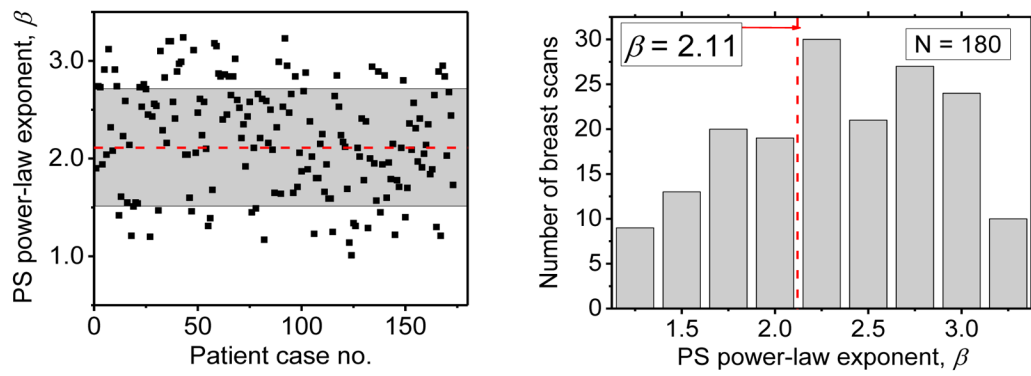
Figure 4.
a) β values of the 180 breast cases acquired with the UCDMC scanner and calculated with the method described in section 2.5. The dashed line and the light grey area represent the mean and the range of $\pm$ 1 std. dev. of these values. b) Frequency histogram of β values for the UCDMC dataset ($N = 180$).
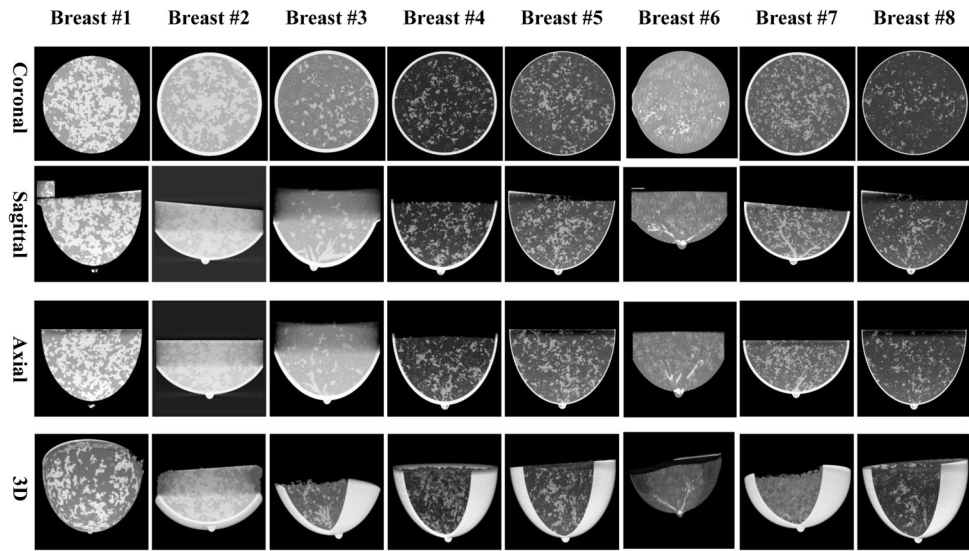
Figure 5.
Example of coronal (a), sagittal (b) axial (c) reconstructed CT slices and a 3D rendering (d) for breast models obtained with *BreastSimulator* software package. These images were obtained simulating the 80 kV setup of the UCDMC scanner.
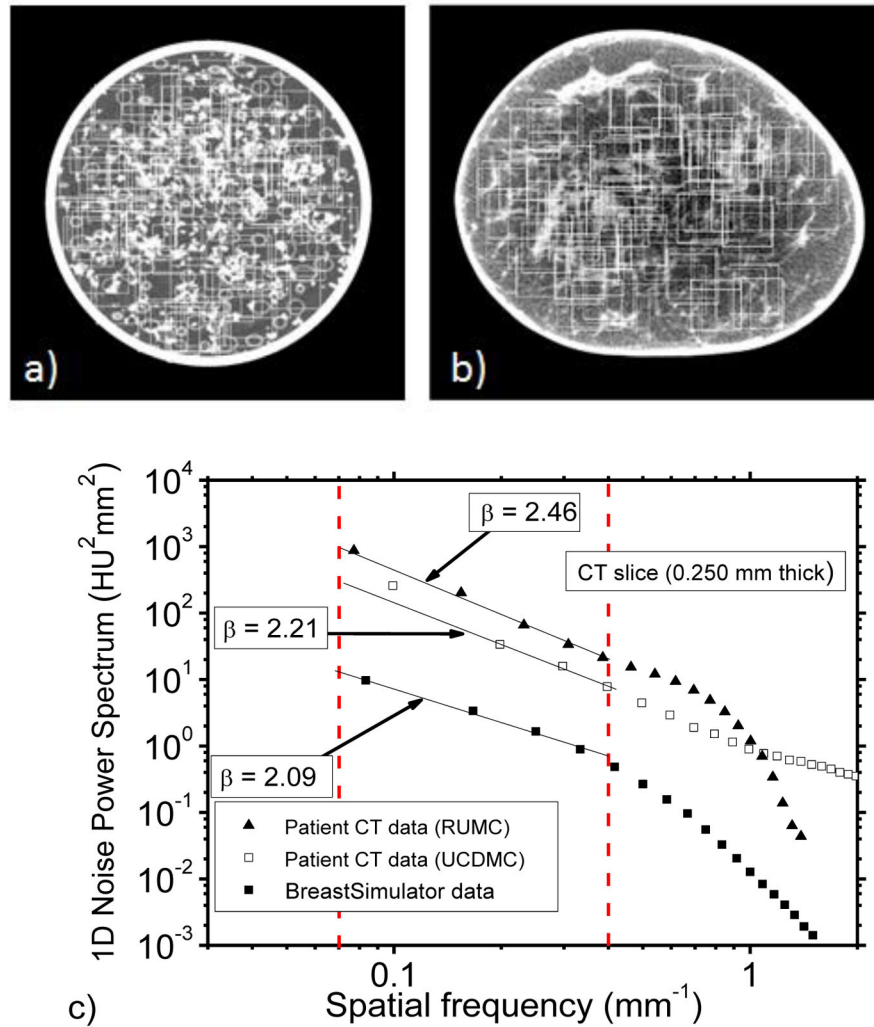
Figure 6.
a) Example of the square ROI sampling carried out on an X-ray reconstructed coronal slice obtained with *BreastSimulator* software and b) on a real breast acquired with the RUMC scanner (@49 kVp). c) The PS evaluated from a single illustrative simulated CT dataset (closed squares) and from a single breast CT scan acquired with the UCDMC scanner (@80 kVp, open squares) and from the RUMC scanner (closed triangles). The continuous lines represent linear fits to the data points in the range 0.05–0.4 mm^{-1}, with the value of corresponding slopes indicated as β values for each dataset. The β coefficients were calculated on the mid-position (from chest wall to nipple) coronal CT slice. The vertical dashed lines indicate the frequency region for calculation of β.
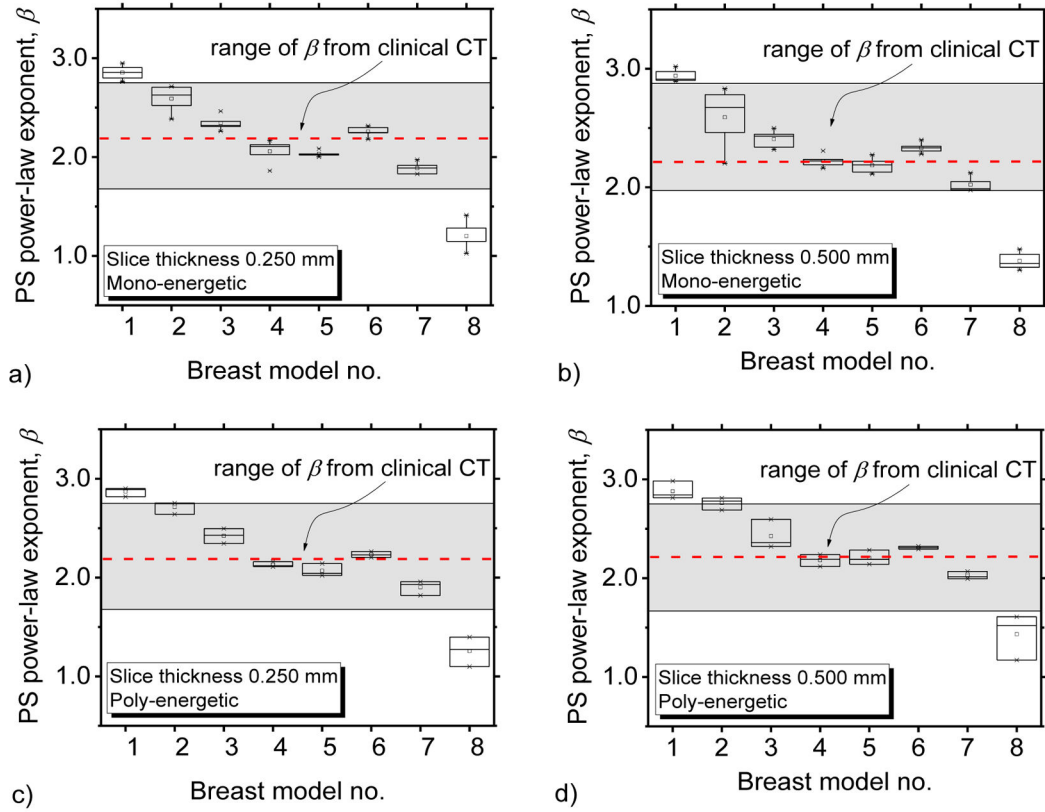
Figure 7.
β coefficients calculated in the central (from chest wall to nipple) coronal slice for each phantom described in tab. I and for mono-energetic (27, 32, 35, 43, 51 keV) (a,b) and poly-energetic (49, 60, 80 kVp) (c,d) X-ray spectra. The slice thickness is (a, c) 0.250 mm or (b, d) 0.500 mm. Each box in the plots indicates mean, median, min, max, and 10th, 25th, 75th and 90th percentile value. The area shaded in light gray represents the mean (dashed red line) $\pm$ 1 std. dev. of the parameter β measured on clinical CT data reported by UCDMC on 185 breast images [Chen *et al* 2013]. Breast models from #2 to #7 are considered to match the range of values found in CT scans of patients' breasts.

Figure 8.
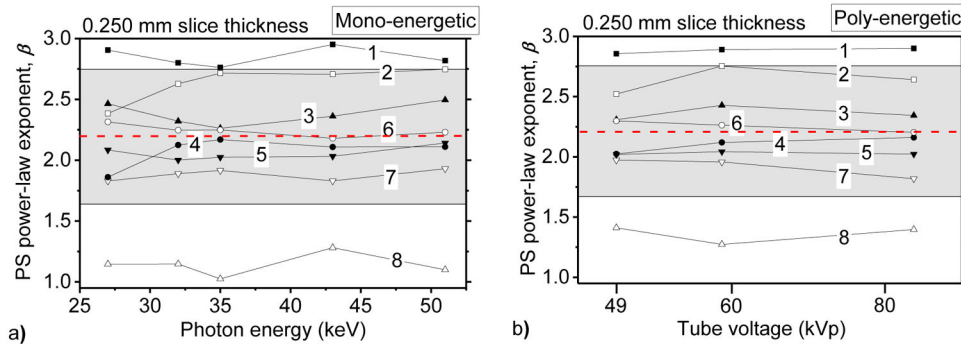Coefficients β calculated in the central coronal slice (of thickness 0.250 mm) for breast models #1 to #8 described in Tab. I, as a function of photon energy, for (a) mono-energetic beams or (b) for poly-energetic beams. The area shaded in light gray represents the mean (dashed red line) ± 1 std. dev. of the parameter β measured on clinical CT data reported by UCDMC on 185 breast images [Chen *et al* 2013].
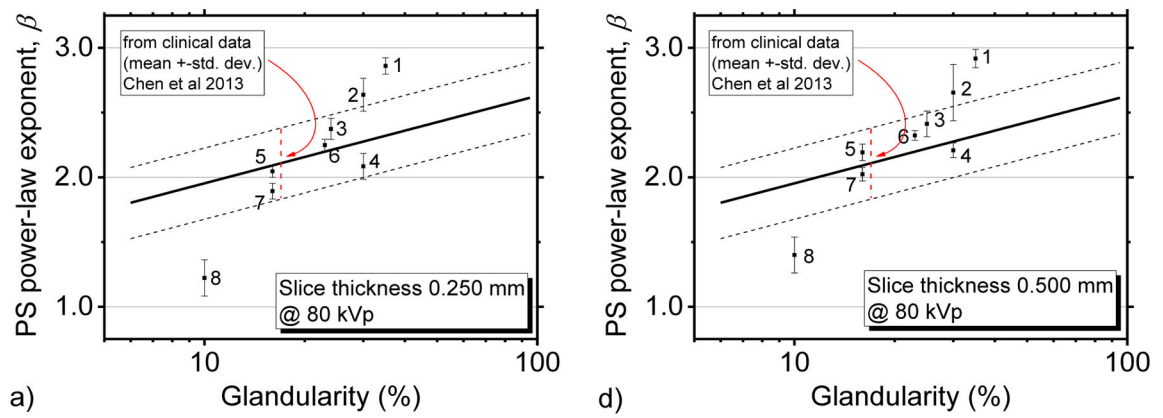
Figure 9.
Coefficients β calculated in the central coronal slice of thickness 0.250 mm (a) and 0.500 mm (b) for breast models #1 to #8 described in Tab. I, as a function of glandularity. The continuous and dashed lines in the figure show the fitted value and range of ± 1 std. dev. reported in Chen *et al.* 2013.
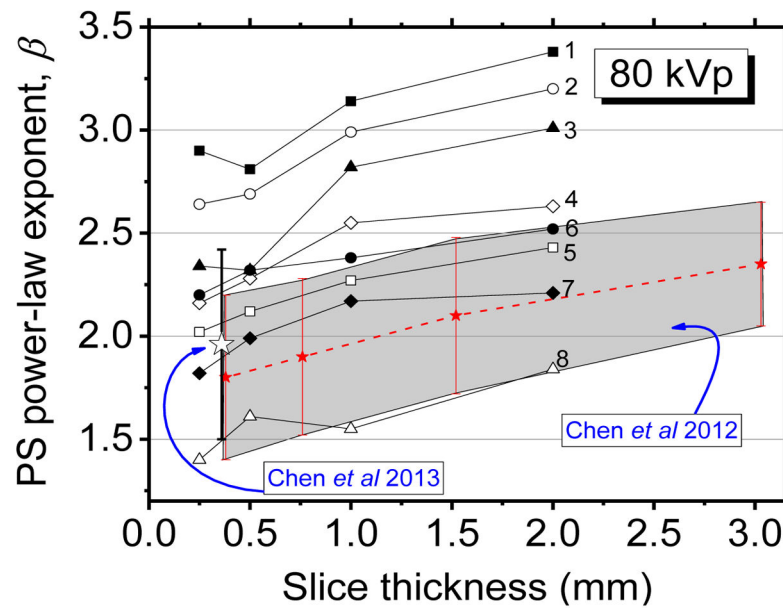
Figure 10.
Coefficients β calculated in the central coronal slice for breast models #1 to #8 described in Tab. I, as a function of slice thickness @80 kVp. The area shaded in light gray represents the values (dashed red line) ± std. dev. of the parameter β measured on clinical CT data reported by UCDMC on 44 breast images [Chen *et al* 2012]. The white star indicates the value of the parameter β measured on clinical CT data reported by UCDMC on 185 breast images [Chen *et al* 2013].
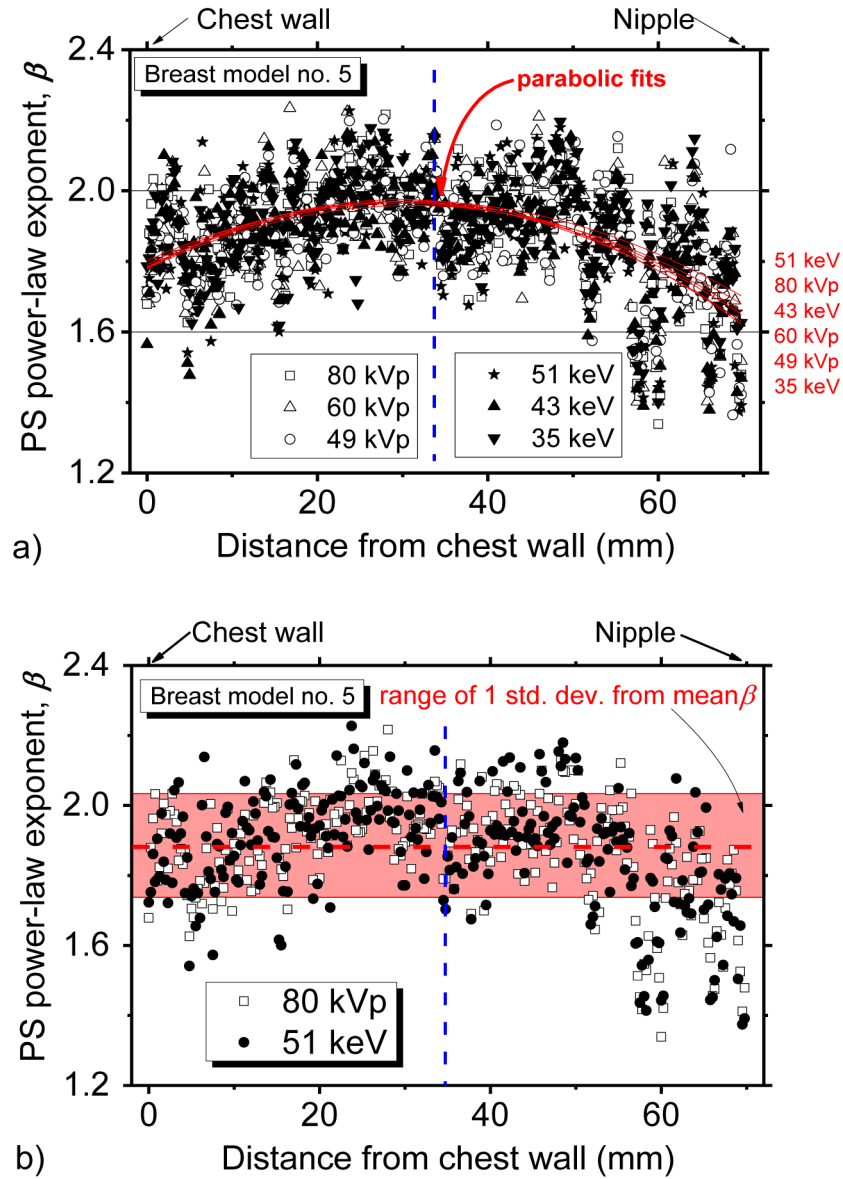
Figure 11.
Power-law exponent β calculated on coronal slices (0.250 mm thick) of simulated CT scans for the breast model #5, as a function of the distance from the chest wall, for (a) all six beam qualities, and (b) for a mono-energetic (51 keV) and a poly-energetic (80 kVp) spectrum. The six quadratic fit lines (in red) in a) show a decreasing trend of β at the sides of the chest wall and nipple. The order of the six fitting curves is indicated on the right side of the plot. In b), the horizontal dashed line and continuous lines (in red) represent the mean value and the (mean±standard deviation) values of the values of β calculated for the two datasets. The dashed vertical line (in blue) in the two plots marks the longitudinal position of the central slice.
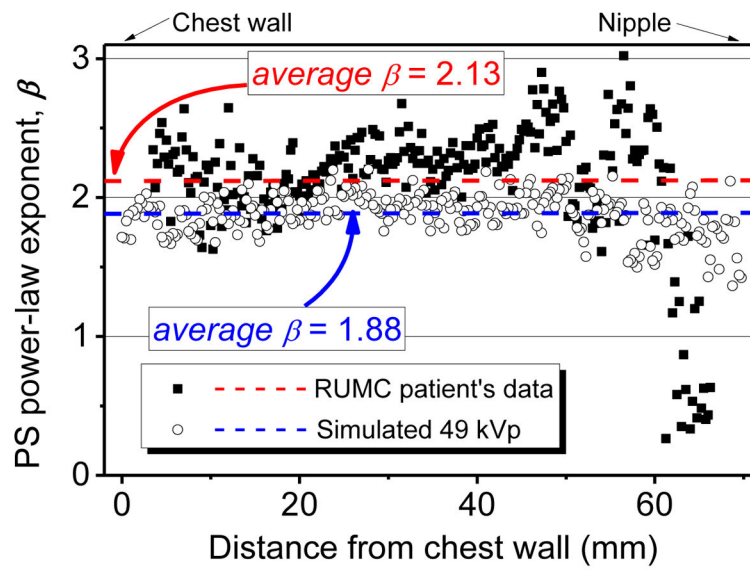
Figure 12.
Coefficient β as a function of the chest-wall distance for the simulated breast model #5 with a poly-energetic beam (49 kVp) (closed symbols) and for a randomly selected RUMC patient's dataset from a dedicated CT scanner (open symbols). The red and the blue dashed lines indicate the average values (2.13 and 1.88 for patient and simulated data, respectively) of β calculated from data in the whole range of distances from the chest wall.

TAB. I

Main features of the eight breast models. The breast size is expressed as the product of three half axes.

	Breast #1	Breast #2	Breast #3	Breast #4	Breast #5	Breast #6	Breast #7	Breast #8
Matrix Size (voxel)	$(800)^3$	$(560)^3$	$(600)^3$	$(1000)^3$	$(1000)^3$	$(1000)^3$	$(1000)^3$	$(700)^3$
Voxel size (mm)	$(0.2)^3$	$(0.25)^3$	$(0.25)^3$	$(0.15)^3$	$(0.16)^3$	$(0.16)^3$	$(0.15)^3$	$(0.1)^3$
Glandularity (%)	35	30	24	30	16	23	16	10
Breast size (mm³)	$60 \times 60 \times 83$	$70 \times 70 \times 60$	$70 \times 70 \times 100$	$60 \times 60 \times 83$	$60 \times 60 \times 83$	$60 \times 60 \times 83$	$70 \times 60 \times 60$	$40 \times 40 \times 40$
Volume (mm³)	6.8×10^5	4.7×10^5	8.5×10^5	5.9×10^5	6.3×10^5	6.3×10^5	4.6×10^5	1.4×10^5
No. Major ducts	4	4	5	5	5	5	5	5
Duct height (mm)	1	1	1	1	1	1	1	1
Duct radius (mm)	2	2	2	2	2	2	2	2
No. Lactiferous ducts	4	4	5	4	5	4	5	5
Lactiferous duct min-max length (mm)	2.0–8.0	2.0–7.0	5.0–13.0	2.0–8.0	2.2–6.0	2.0–8.0	2.5–9.0	2.2–6.2
Lactiferous duct radius (mm)	0.12	0.12	0.15	0.12	0.12	0.12	0.20	0.12
No. Cooper Ligaments	300	300	1100	1500	1000	1500	8000	12000
Cooper Ligaments radius (mm)	2.5	4.0	3.0	2.0	3.0	2.0	2.5	2.5

Table II

Power-law exponent β calculated from simulated breast models (#1 to #8) and measured from central coronal slices of clinical CT scans, for mono-energetic and poly-energetic X-ray beams. The parameter ϕ is the thickness of the slice used for calculation of the β parameter.

Breast model	ϕ (mm)	Mono-energetic					Poly-energetic		
		27 keV	32 keV	35 keV	43 keV	51 keV	49 kVp	60 kVp	80 kVp
#1	0.25	2.90±0.76	2.80±0.66	2.76±0.72	2.95±0.78	2.82±0.76	2.85±0.73	2.89±0.74	2.90±0.63
	0.50	2.89±0.74	2.90±0.97	2.91±0.61	2.98±0.56	2.98±0.87	3.02±0.82	2.84±0.93	2.81±0.83
	1	3.10±0.90	3.11±1.02	3.22±0.83	3.12±0.89	3.17±0.81	3.07±0.77	3.07±0.76	3.14±0.93
	2	3.26±0.88	3.33±1.08	3.43±0.73	3.38±0.60	3.36±0.82	3.36±0.72	3.41±0.58	3.38±0.70
#2	0.25	2.38±0.09	2.63±0.28	2.71±0.22	2.71±0.42	2.74±0.35	2.52±0.18	2.75±0.48	2.64±0.25
	0.50	2.20±0.36	2.67±0.41	2.83±0.67	2.78±0.46	2.78±0.50	2.46±0.44	2.81±0.47	2.69±0.74
	1	2.47±0.14	2.96±0.42	3.01±0.43	2.95±0.52	3.06±0.41	2.84±0.40	2.99±0.39	2.99±0.62
	2	2.52±0.50	2.95±0.37	3.13±0.28	3.20±0.72	3.23±0.34	2.93±0.23	3.20±0.29	3.20±0.39
#3	0.25	2.46±0.20	2.32±0.38	2.26±0.47	2.36±0.33	2.49±0.27	2.31±0.27	2.43±0.31	2.34±0.24
	0.50	2.34±0.32	2.45±0.53	2.43±0.27	2.32±0.42	2.59±0.24	2.50±0.53	2.36±0.51	2.32±0.29
	1	2.74±0.38	2.83±0.60	2.72±0.32	2.91±0.43	2.76±0.49	2.58±0.50	2.94±0.52	2.82±0.49
	2	3.06±0.48	3.05±0.57	3.10±0.67	3.22±0.84	3.14±0.34	2.91±0.58	3.19±0.53	3.01±0.51
#4	0.25	1.86±0.70	2.12±0.94	2.17±0.51	2.11±0.80	2.11±0.97	2.02±0.67	2.12±0.51	2.16±0.74
	0.50	2.16±0.62	2.31±0.87	2.23±0.98	2.19±0.86	2.24±0.92	2.22±0.94	2.19±0.79	2.12±1.02
	1	2.28±0.84	2.49±0.77	2.38±0.56	2.37±0.61	2.47±0.72	2.32±0.62	2.44±0.54	2.55±0.48
	2	2.55±0.80	2.63±0.47	2.66±0.61	2.64±0.34	2.61±0.73	2.59±0.66	2.63±0.35	2.63±3.06
#5	0.25	2.08±0.89	2.00±0.94	2.02±0.93	2.03±1.07	2.14±0.85	2.02±1.16	2.04±0.95	2.02±1.05
	0.50	2.11±0.78	2.13±0.99	2.22±0.84	2.27±0.70	2.14±1.00	2.19±0.76	2.19±1.14	2.28±1.00
	1	2.24±1.00	2.38±0.93	2.22±1.26	2.25±0.77	2.23±1.08	2.24±1.34	2.33±1.01	2.27±1.10
	2	2.38±0.86	2.39±0.97	2.35±1.08	2.32±1.08	2.38±0.92	2.31±0.71	2.38±1.17	2.43±0.86
#6	0.25	2.31±0.84	2.25±0.76	2.25±0.75	2.18±0.61	2.23±0.94	2.30±0.85	2.26±0.68	2.20±0.86
	0.50	2.30±0.97	2.28±0.73	2.33±0.76	2.35±0.90	2.31±0.84	2.40±0.99	2.29±0.93	2.32±0.99
	1	2.36±1.04	2.33±0.98	2.44±0.87	2.49±0.81	2.53±0.98	2.40±0.98	2.28±0.88	2.38±0.71

Breast model	φ (mm)	Mono-energetic					Poly-energetic		
		27 keV	32 keV	35 keV	43 keV	51 keV	49 kVp	60 kVp	80 kVp
	2	2.58±0.96	2.49±1.10	2.59±0.67	2.58±0.70	2.54±0.78	2.54±0.68	2.56±0.82	2.52±0.86
#7	0.25	1.83±0.48	1.89±0.31	1.91±0.13	1.83±0.64	1.93±0.43	1.97±0.49	1.96±0.31	1.82±0.36
	0.50	1.98±0.44	1.99±0.47	1.97±0.51	2.12±0.37	2.07±0.62	2.05±0.57	2.01±0.69	1.99±0.57
	1	2.23±0.67	2.26±0.54	2.08±0.56	2.20±0.38	2.12±0.57	2.08±0.51	2.09±0.77	2.17±0.49
	2	2.10±0.51	2.18±0.91	2.31±0.86	2.14±0.77	2.22±0.99	2.29±0.69	2.19±0.71	2.21±0.82
#8	0.25	1.15±0.44	1.14±0.50	1.02±0.66	1.28±0.35	1.10±0.44	1.41±0.60	1.27±0.39	1.40±0.28
	0.50	1.43±0.22	1.32±0.52	1.36±0.53	1.47±0.15	1.17±0.47	1.30±0.62	1.52±0.46	1.61±0.21
	1	1.47±0.34	1.40±0.16	1.50±0.27	1.40±0.42	1.46±0.22	1.55±0.28	1.38±0.46	1.55±0.35
	2	1.85±0.43	1.83±0.32	1.70±0.31	1.74±0.20	1.72±0.14	1.81±0.30	1.75±0.18	1.84±0.48
RUMC scanner							2.15±0.36		
UCDMC scanner									2.21±0.55